ACS APPLIED ELECTRONIC MATERIALS

pubs.acs.org/acsaelm Article

Design, Fabrication, and Performance Analysis of TiO_2 Detector Prototype for X-ray Detection Application

Rupa Jeena, Parushottam Majhi,* Saikat Mitra, Pankaj Chetry, Kantimay Das Gupta, and Pradeep Sarin

Cite This: *ACS Appl. Electron. Mater.* 2025, 7, 5322−5330 Read Online

ACCESS | Metrics & More | Article Recommendations | Supporting Information

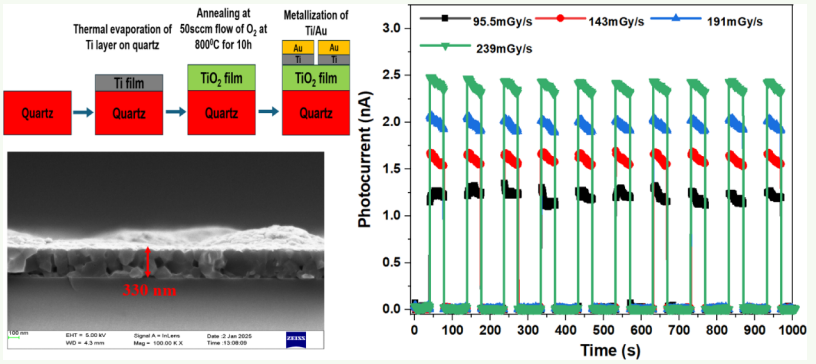

ABSTRACT: This study demonstrates the potential of TiO_2, a wide bandgap semiconductor, for the detection of X-rays with an energy of ∼8 keV based on its photocurrent response. A TiO_2 film ∼ 330 nm thick was synthesized using the thermal oxidation technique. Titanium/gold (Ti/Au) metallic contact pads were deposited on its top surface in a metal-semiconductor-metal (MSM) configuration. The active channel length between the pads is 120 μm. Comprehensive material characterization of the TiO_2 was conducted using X-ray diffraction (XRD) and laser Raman spectroscopy (LRS), confirming the presence of the purely rutile TiO_2 phase in the fabricated film. Spectroscopy showed strong UV absorption in the 300 to 370 nm range, with an optical bandgap of approximately 3.1 eV. Atomic force microscopy (AFM) and scanning electron microscopy (SEM) were utilized to analyze the morphology of the film, indicating the formation of a compact and dense structure with a surface roughness of 36 nm. Dark IV measurements showed that the device is highly resistive, with resistivity in the range of 10^{12} Ω·cm. X-ray detection performance of the detector was evaluated under varying X-ray dose rates and bias voltages, demonstrating a linear correlation between photocurrent, dose rate, and bias voltage. Repeatability was confirmed through ten cycles of response measurements at different dose rates, ensuring consistent performance. The device exhibited reliable, efficient, and repeatable X-ray detection with an excellent response and recovery characteristics. These findings highlight the promise of TiO_2-based detectors for X-ray imaging, medical diagnostics, environmental monitoring, and advanced X-ray sensing applications.

KEYWORDS: *oxide electronics, photodetector, TiO_2, wide bandgap semiconductors, X-ray detection*

1. INTRODUCTION

The detection of X-ray radiation is essential across various fields, including scientific research, material characterization, medical imaging, security screening, industrial inspection, astronomy, and space communication.[1−6] X-ray detectors are broadly categorized into indirect and direct detection systems.[7,8] Indirect detection utilizes scintillators that convert X-rays into lower-energy photons, which are then detected by photodetectors.[9−11] While widely adopted, this approach has limitations such as low energy resolution, slower response time, limited sensitivity, and optical crosstalk.[12,13] In contrast, direct X-ray detection employs photoconductive materials that directly convert X-ray photons into electrical signals. It minimizes optical losses, improves image resolution, simplifies the system, and enables real-time imaging. As a result, significant research has been focused on developing direct detection technologies that address the shortcomings of indirect detection systems.[14−18] Currently, solid-state direct X-ray detectors primarily utilize semiconductor materials such as silicon, germanium, amorphous selenium, and cadmium zinc telluride (CZT) due to their impressive detector performance response.[19−23] However, these materials present certain challenges. For instance, CZT detectors require high operating voltage (>500V) and have limitations in pixel size. Amorphous

Received: April 14, 2025
Revised: May 6, 2025
Accepted: May 7, 2025
Published: May 21, 2025

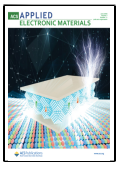

https://doi.org/10.1021/acsaelm.5c00757
ACS Appl. Electron. Mater. 2025, 7, 5322−5330

selenium-based X-ray detectors exhibit low X-ray attenuation for energies exceeding 50 keV, while silicon and germanium are susceptible to radiation damage. To address these limitations, wide-bandgap semiconductors have emerged as promising candidates for next-generation X-ray detectors. Their unique attributes, including a bandgap greater than 2.3 eV, high radiation tolerance, high breakdown voltage, good absorption for X-ray, and cost-effectiveness, make them promising candidates for X-ray detection applications.[24] In recent years, advanced X-ray detectors have been developed using materials such as gallium oxide (Ga_2O_3), zinc oxide (ZnO), lead oxide (PbO), mercury iodide (HgI_2), diamond, silicon carbide (SiC), lead iodide (PbI_2), bismuth oxide (Bi_2O_3), and indium−gallium−zinc oxide (IGZO).[25−33]

When an X-ray photon beam passes through a material, it interacts with the material and undergoes attenuation due to absorption or scattering, leading to a decrease in beam intensity. The attenuation coefficient depends on the X-ray energy (E) and the effective atomic number (Z) of the material, following the relation Z^4/E^3. High-Z materials such as HgI_2, PbI_2, PbO, BGO, and Bi_2O_3, which are commonly used in X-ray detectors, have higher attenuation coefficients than other materials.

However, the search for X-ray detector materials extends beyond high-Z semiconductors, focusing on the development of cost-effective and environmentally friendly alternatives that offer long-term stability and compatibility with scalable fabrication techniques. In this context, titanium dioxide TiO_2 stands out as a promising but underexplored option. Although it is widely used in photocatalysis[34,35] and UV detection,[36−38] its potential for X-ray detection has received little attention, creating an opportunity for further research. TiO_2 is a wide bandgap semiconductor and exists in three crystalline phases: rutile, anatase, and brookite, with rutile being the most thermodynamically stable.[39,40] Depending on its phase, TiO_2 exhibits a bandgap ranging from 3.0 to 3.6 eV[41−43] ensuring high resistivity and minimal leakage current, which are advantageous for photodetector applications. Furthermore, its low dark current enhances the signal-to-noise ratio, making it well-suited for ionizing radiation detection.[44] Additionally, TiO_2 demonstrates remarkable stability in high-radiation environments, reinforcing its potential in radiation detection technologies. Moreover, unlike heavy metal-based semiconductors such as PbI_2, HgI_2, and CdTe, TiO_2 is nontoxic, biocompatible, and environmentally friendly, making it a safer alternative for medical imaging, space applications, and environmental monitoring.

In this work, we have prepared a TiO_2 film using a simple and cost-effective thermal oxidation technique. The material preparation process is described, followed by an in-depth analysis of material characterization using various analytical techniques. The study also includes electrical characterization, such as dark current-voltage (I-V) measurements and detector response under X-ray exposure at different dose rates and biasing conditions. Finally, the conclusion and future prospects of this research are discussed.

2. EXPERIMENTAL SECTION

2.1. Film Preparation. The fabrication process begins with precleaning the quartz substrate (dimensions: 1 cm × 1 cm × 0.1 cm) using detergent, followed by ultrasonic cleaning in sequential steps with acetone, isopropyl alcohol (IPA), and deionized (DI) water for 5 min each. After cleaning, the substrate is dried using a nitrogen flow and heated at 125° C for 5 min to eliminate any residual contaminants. Next, the substrate is placed in a thermal evaporator (Smart Coat 3.0) for the deposition of Ti using high-purity Ti wire (99.99%, Alfa Aesar) as the source material. The Ti deposition is conducted under high vacuum conditions ($<10^{-7}$ mbar), with the film thickness continuously monitored using a quartz crystal monitor (QCM). The entire procedure of Ti deposition is repeated to increase the film thickness. Repetition of the process is necessary due to a system limitation in depositing only about 100 nm of Ti in thermal evaporation at one time. To convert the Ti film into TiO_2, the deposited film is then loaded into a tubular quartz furnace for annealing in oxygen. The temperature is ramped up at a controlled rate of 13° C/min to 800° C, where it is maintained for 10 h. During the annealing process, a continuous oxygen flow of 50 SCCM is supplied. The schematic illustration in Figure 1 depicts the complete process, from film fabrication to the deposition of metallic contact pads. The prepared film is characterized using various analytical techniques, including X-ray diffraction (XRD), laser Raman spectroscopy (LRS), scanning electron microscopy (SEM), atomic force microscopy (AFM), and UV−visible spectroscopy. These techniques are employed to study the structural, phase identification, morphological, and optical properties of the films.

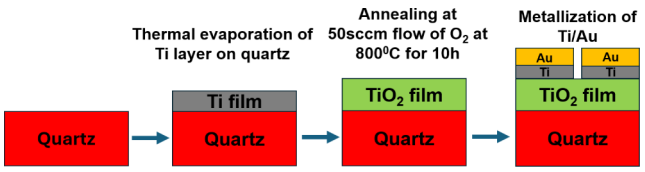

Figure 1. Schematic representation of the film fabrication process.

2.2. Film Characterizations. The structural properties and phase identification of the film were analyzed by using X-ray diffraction (XRD) and laser Raman spectroscopy (LRS). High-resolution XRD data were obtained by using a PANalytical Empyrean XRD system equipped with a Cu anode rod. The film was scanned over a 2θ range of 10° to 90° using Cu−Kα radiation (λ = 1.54 Å) to determine its crystal structure and phase composition. LRS was conducted by using an HR800UV confocal micro-Raman spectrometer (Horiba Jobin Yvon) with a 532 nm excitation wavelength. This technique complemented the XRD analysis by providing insights into the vibrational modes of the material and confirming the phase of the film. The surface morphology of the film was examined using scanning electron microscopy (SEM) with a Zeiss Ultra 55 setup. Additionally, atomic force microscopy (AFM) analysis was performed using the Asylum Research MFP-3D BIO system to evaluate the surface roughness at the nanoscale. The optical properties of the film were characterized by using a PerkinElmer Lambda 950 UV−visible spectrometer. The UV−visible measurements provided crucial information about the optical bandgap, transparency, and absorption characteristics of the film.

2.3. Device Fabrication. To study the electrical characteristics, Ti/Au contacts with thicknesses of 20 and 80 nm, respectively, are deposited on the surface of the TiO_2 film in a metal semiconductor-metal (MSM) configuration, with an active channel of 120 μm length between the electrodes. Ti serves as a buffer layer, providing a stable interface by adhering well to the TiO_2 film, while Au establishes contact with Ti, ensuring efficient charge transport, electrical conductivity, and long-term stability of the contact. The metallization of Ti/Au contacts is carried out using a thermal evaporator under high vacuum ($<10^{-7}$ mbar), ensuring uniformity and precise deposition of reliable metallic electrical contacts.[45] The device is subsequently tested for both DC and AC electrical measurements, enabling a comprehensive analysis of its electrical properties.

3. RESULTS AND DISCUSSION

3.1. Structural, Morphological, and Optical Properties. Figure 2a presents the XRD data of the film, revealing

https://doi.org/10.1021/acsaelm.5c00757
ACS Appl. Electron. Mater. 2025, 7, 5322−5330

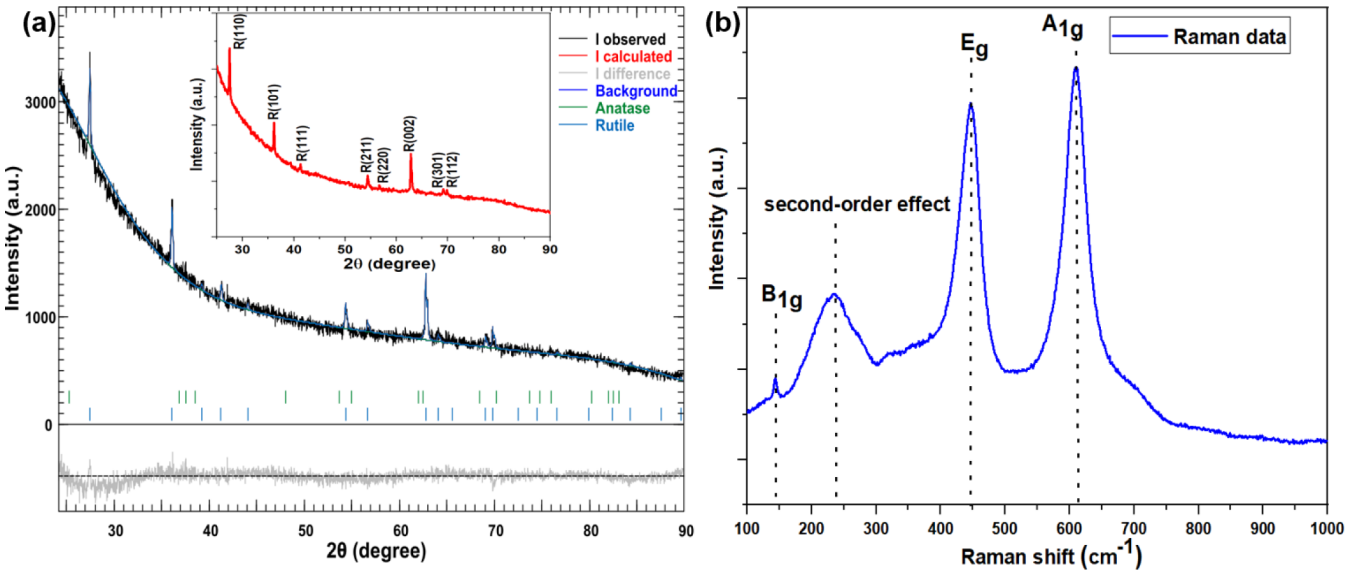

Figure 2. (a) Rietveld refinement analysis of the TiO_2 film is presented, with the inset displaying XRD data confirming the formation of the polycrystalline rutile phase. (b) Laser Raman analysis of the film is performed to investigate its vibrational modes using a 532 nm excitation wavelength.

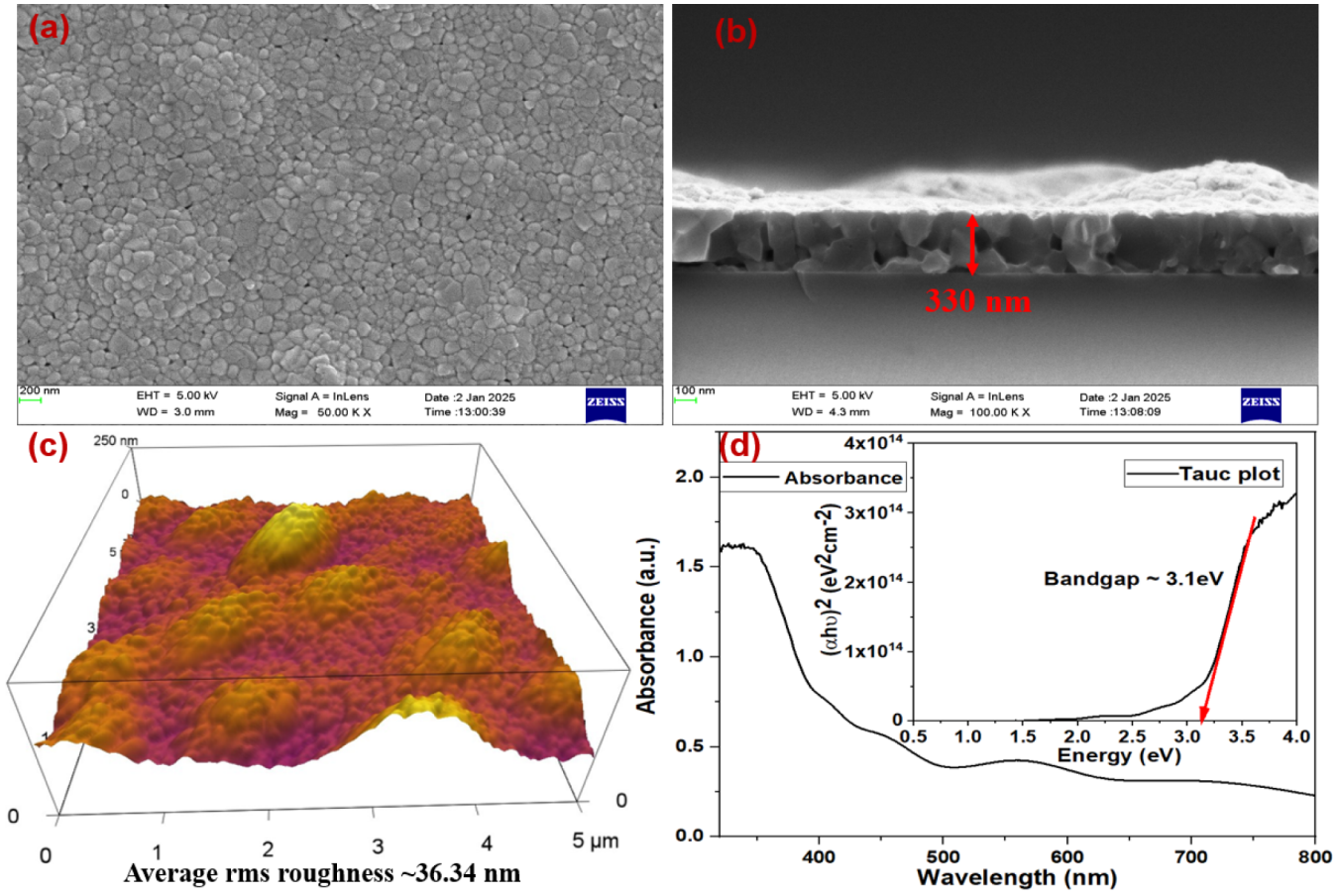

Figure 3. Morphological and optical characterizations of the film. (a) The top-view SEM image of the film indicates the formation of a high-quality, uniform, and compact film. (b) The cross-sectional image informs a film thickness of approximately 330 nm. (c) The 3D AFM image (scan range: 5 μm × 5 μm) demonstrates the presence of a compact film. (d) The absorption data of the film indicate the absorption region in the UV range, while the inset shows the optical bandgap of the material calculated ~ 3.1 eV.

well-defined diffraction peaks corresponding to the R (110), R (101), R (111), R (211), R (220), R (002), R (301), and R (112) planes. These peaks are identified by referencing JCPDS file 021-1276 for the rutile phase of TiO_2. The Rietveld refinement of the XRD analysis provides strong confirmation of the complete formation of the rutile phase, with no

https://doi.org/10.1021/acsaelm.5c00757
ACS Appl. Electron. Mater. 2025, 7, 5322−5330

observable peaks associated with metallic Ti or other TiO_2 polymorphs, such as anatase.[46] The average grain size of the film, estimated using the Scherrer formula,[47] is found to be in the range of 25−30 nm. Following the structural and crystallinity analyses, the vibrational modes of the film were investigated using Raman spectroscopy with an excitation wavelength of 532 nm. The Raman spectrum, shown in Figure 2b, displays prominent peaks at approximately 145 cm^{-1}, 236 cm^{-1}, 445 cm^{-1}, and 610 cm^{-1}, corresponding to the characteristic Raman active modes of rutile TiO_2: B_{1g}, second-order effect, E_g, and A_{1g}, respectively.[48]

The top-view SEM image, shown in Figure 3a, reveals the formation of a smooth, uniform, high-quality, and compact film with no visible cracks. The film thickness is measured to be approximately 330 nm, as observed in the cross-sectional SEM image in Figure 3b. The layer-by-layer deposition of Ti, followed by oxygen annealing, ensures a uniform structure without the formation of cracks. While some regions exhibit nucleation growth, the overall film remains continuous. Further surface characterization is performed using atomic force microscopy (AFM). The AFM scan of a 5 μm × 5 μm region, shown in Figure 3c, provides additional insight into the surface morphology. The film appears dense and uniform, with an average surface roughness of approximately 36.34 nm. The optical properties of the film are investigated by using UV−visible spectroscopy. A detailed optical analysis, including absorption spectra and optical bandgap estimation via Tauc plotting, is conducted. The absorption spectra exhibit strong absorption in the UV region (300−370 nm), as depicted in Figure 3d. The Tauc plot analysis determines a direct optical bandgap of approximately 3.1 eV, which is consistent with previously reported values for TiO_2 films synthesized through various deposition techniques.[42]

3.2. Electrical Characterizations. *3.2.1. Dark IV Measurement of the Sample.* The IV measurement of the device is performed under high vacuum conditions using a Keithley 6487 source meter. As shown in Figure 4, the IV characteristic exhibits linear behavior, indicating good ohmic contact formation. The measurement is performed by varying the bias voltage from −20 to 20 V, resulting in a dark current of ∼80 pA at 20 V. Based on the dark I-V measurement results, the resistance and resistivity are determined to be 0.25 × 10^{12} Ω and 1.57 × 10^{12} Ω·cm, respectively. The calculated resistivity value is generally consistent with previously reported values for TiO_2 obtained through various fabrication approaches.[49] Since noise amplitude largely depends on the dark current, the high resistivity helps minimize the dark current, effectively reducing noise.[50]

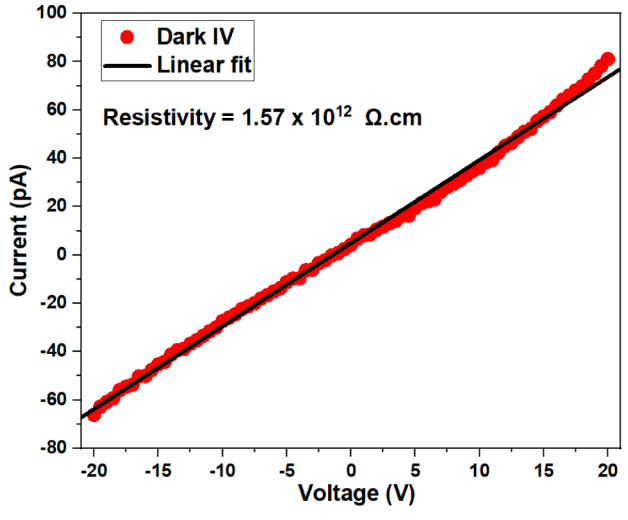

Figure 4. Dark I-V characteristics of the device.

3.2.2. X-ray Detection Mechanism in Semiconductors. X-ray radiation interacts with semiconductor materials through various mechanisms, including photoelectric effects, Compton scattering, and pair production. The dominant process responsible for electron−hole pair (EHP) generation depends on the incident X-ray energy. For X-ray energies up to 500 keV, the photoelectric effect is the primary interaction mechanism.[51] In this process, an X-ray photon transfers its energy to an atomic electron, ejecting it from its orbital and creating a vacancy, resulting in atomic ionization. This vacancy is subsequently filled by an electron transitioning from a higher energy level, releasing energy in the form of either characteristic X-ray photons or Auger electrons. If characteristic X-rays are reabsorbed by nearby atoms, they can trigger additional ionization, while Auger electrons due to their high energy contribute to further electronic excitations. However, it is important to distinguish between the classical photoelectric effect, where an electron is ejected into a vacuum, and photoexcitation, where electrons remain within the material. In X-ray interactions with semiconductors, the generated secondary electrons primarily move to the conduction band rather than escape into a vacuum, making this process different from the conventional photoelectric effect. Electron escape to a vacuum occurs only within a very shallow region (10 nm). Deeper electrons lose energy through inelastic scattering with the lattice before reaching the surface, preventing their direct escape. As a result, the low-energy secondary electrons move toward the conduction band (CB), while holes migrate toward the valence band (VB). Under an applied bias, these charge carriers drift toward the electrodes, where they are collected to generate an electrical signal. The number of EHPs generated is directly proportional to the absorbed X-ray energy, influencing the sensitivity and efficiency of the detector.[24]

3.2.3. Response of the Sample under X-ray Exposure. The X-ray detection study is performed by placing the sample inside a custom-designed chamber, where X-rays of energy (∼8 keV) with varying dose rates are directed onto the active region of the film. Details of the photocurrent measurement procedure under X-ray irradiation are provided in Figure S1. The study investigates the response of the detector under different X-ray dose rates and bias voltages, providing a comprehensive evaluation of its performance under various operational conditions.

The response of the detector to X-ray exposure is measured at two different dose rates (143 and 191 mGy/s) while gradually increasing the bias voltage. Figure 5 presents the photocurrent response for five min duration at these dose rates under various bias conditions. The data indicate that the current increases with both the applied voltage and the X-ray dose rate. However, the photocurrent initially rises before gradually decaying over time. This behavior is attributed to charge carrier dynamics, including their generation, transport, and recombination. Upon X-ray irradiation, a significant number of electron−hole pairs and energetic secondary electrons are generated. The initial drift of these carriers toward the electrodes leads to a rise in photocurrent. However, over time, polarization effects within the detector become

https://doi.org/10.1021/acsaelm.5c00757
ACS Appl. Electron. Mater. 2025, 7, 5322−5330

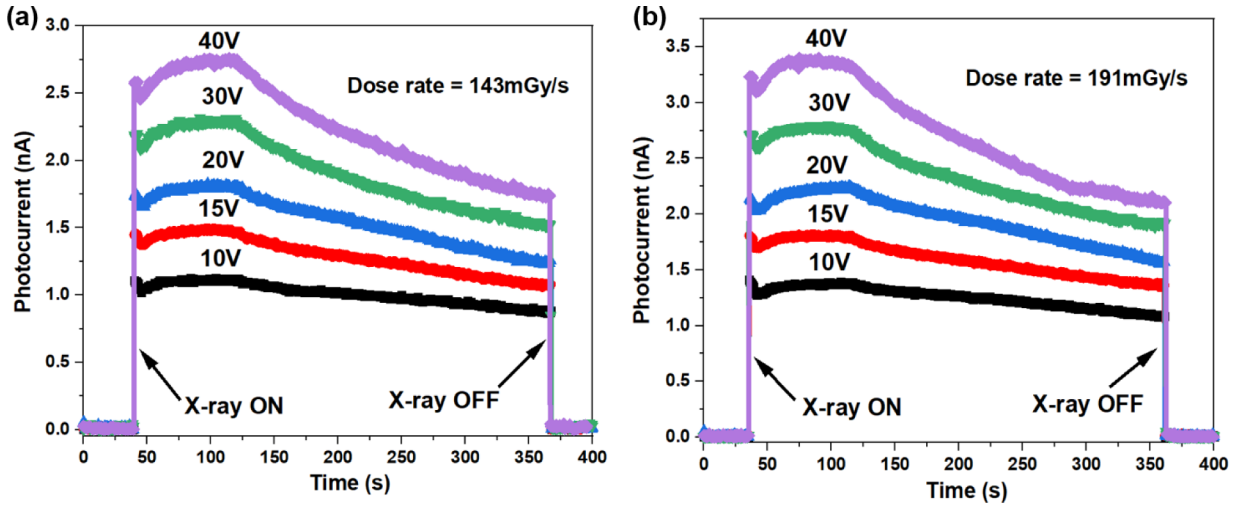

Figure 5. Photoresponse of the detector under two different X-ray dose rates (a) 143 and (b) 191mGy/s with increasing biasing voltage.

more pronounced. Bale and Szeles[52] proposed a dynamic model describing how intense X-ray radiation induces polarization in semiconductors. According to this model, polarization arises due to charge carrier trapping at deep impurity levels, leading to the formation of a high-charge-density space-charge region. This modifies the internal electric field profile. The induced polarization field opposes the externally applied drift field, affecting charge carrier transport. Additionally, the decay in the photocurrent is further influenced by increased carrier recombination through shallow or deep defect states within the material. Similar time-dependent degradation of photoresponse has been observed in other X-ray detector materials, including CZT, HgI_2, and thallium bromide (TlBr).[53]

Using experimental data, we have calculated key parameters of the detector, including sensitivity, responsivity, mobility-lifetime ($\mu\tau$) product, and diffusion length at an X-ray dose rate of 143 mGy/s and an operating voltage of 20 V. Sensitivity measures the charge collected per unit area when the detector is exposed to X-ray photons.[24,54] It is given by

$$S = \frac{I_{\text{X-ray}} - I_{\text{dark}}}{D \cdot A} \tag{1}$$

where $I_{\text{X-ray}}$ is the photocurrent under X-ray exposure, I_{dark} is the dark current, D is the X-ray dose rate, and A is the exposed area of the detector. The calculated sensitivity of the detector is 29.49 μC/mGy/cm^2. The sensitivity values corresponding to other X-ray dose rates are plotted and presented in Figure S2.

Another important parameter is the responsivity, which is calculated using the following formula:[54]

$$R = \frac{I_{\text{X-ray}} - I_{\text{dark}}}{D} \tag{2}$$

The measured responsivity of the device is 1.16×10^{-5} μC/mGy.

Moreover, we have calculated the mobility-lifetime product, a key figure of merit for evaluating the performance of X-ray detectors and comparing different semiconductor materials.[55,56] This parameter indicates how efficiently charge carriers travel through the material under an applied electric field, directly impacting the signal strength and response time. The $\mu\tau$ product of the device is determined by fitting the data to the Hecht equation[57] which describes the charge carrier collection efficiency at the electrodes under an applied bias.

$$I = I_0 \left| \frac{V\mu\tau(1 - e^{-d^2/V\mu\tau})}{d^2} \right| \tag{3}$$

I defines the photocurrent, I_0 denotes the saturated photocurrent, V is the bias voltage, and d is the distance between the electrodes or the channel length. By evaluating the response of the detector at different bias voltages, as shown in Figure 6, the average $\mu\tau$ product at a dose rate of 143 mGy/s is calculated to be 2.77×10^{-6} cm^2/V.

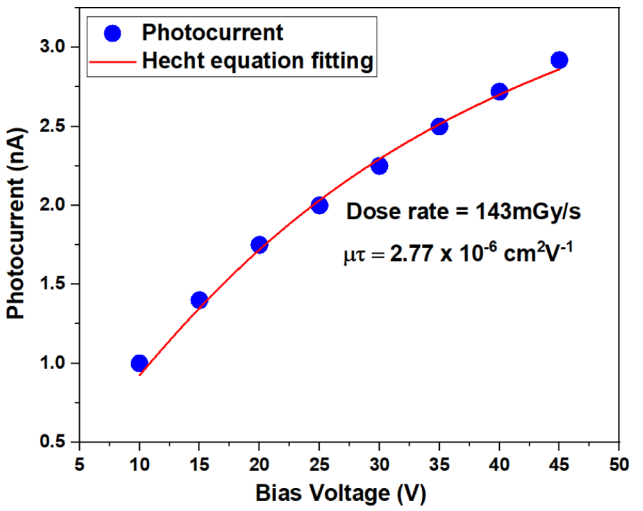

Figure 6. Calculation of the mobility-lifetime product of the detector.

We have also determined the diffusion length of the charge carriers, which represents the average distance the charge carriers travel before recombination.[58] The diffusion length is given by the following equation.

$$L_D = \sqrt{D\tau} \tag{4}$$

where D is the diffusion coefficient and τ is the excited charge carrier lifetime. The diffusion coefficient can be defined by the Einstein relation.

https://doi.org/10.1021/acsaelm.5c00757
ACS Appl. Electron. Mater. 2025, 7, 5322−5330

$$D = \frac{\mu k_B T}{q} \quad (5)$$

$$L_D = \sqrt{\left(\frac{\mu \tau k_B T}{q}\right)} \quad (6)$$

In the above equation, $\mu\tau$ represents the mobility-lifetime product, determined using the Hecht equation, k_B is the Boltzmann constant, T denotes the temperature, and q is the charge of an electron. The calculated diffusion length is found to be 2.68 μm. Although this value is smaller than the channel length of the device, charge transport through the material is not entirely governed by carrier diffusion. Instead, it is significantly influenced by drift current, which depends on the applied bias field and becomes the dominant transport mechanism at high bias. Additionally, factors such as scattering, carrier mobility, and trap states within the material further impact the overall transport dynamics and are critical in determining the electrical performance of the device.

The parameters that provide insights into the performance of the detector have been systematically calculated and are presented in Table 1.

Table 1. Summary of Calculated Parameters from X-ray Response Data

Parameters	Units	Values
Dark resistivity	Ω·cm	1.57×10^{12}
Sensitivity	μC/mGy/cm^2	29.49
Responsivity	μC/mGy	1.16×10^{-5}
Mobility-lifetime product	cm^2/V	2.77×10^{-6}
Diffusion length	μm	2.68

Table 2 presents a comparison of sensitivity, responsivity, and the mobility-lifetime product for X-ray detectors based on different semiconductor materials. The data show that the figure of merit of our detector is comparable to the well-established detectors previously used for X-ray detection. This demonstrates the promising performance of our device and highlights its potential for practical use in X-ray sensing applications.

We investigate the response of the detector at four different dose rates: 95.5 mGy/s, 143 mGy/s, 191 mGy/s, and 239 mGy/s while maintaining a fixed bias voltage of 20 V to evaluate signal repeatability, as shown in Figure 7a. The detector undergoes multiple measurement cycles under X-ray exposure, and the data show that the photocurrent remains nearly unchanged and reproduces consistently over 10 cycles, demonstrating the excellent repeatability of the X-ray detector. Additionally, from the data, we analyze the response and recovery behaviors of the detector, which characterize how efficiently the detector responds to X-ray photons and how quickly it returns to the baseline once the X-ray is off. A highly efficient detector should exhibit an immediate increase in photocurrent upon X-ray exposure and a rapid return to its baseline current once the source is turned off. The rapid response and recovery times of the detector demonstrate its capability to function effectively in dynamic environments, where radiation intensity fluctuates frequently. This makes it highly suitable for real-time monitoring applications, where quick adaptation to changing X-ray intensities is crucial for accurate detection and imaging.

We have also plotted the X-ray photocurrent as a function of dose rate to determine the exponent α. The photocurrent follows a power-law relationship with the X-ray dose rate, expressed as $I \propto P_0^{\alpha}$, where P_0 represents the dose rate. The exponent α is obtained from the slope of the linear fit in the log−log plot of the current versus dose rate and is found to be 0.71, as shown in Figure 7b. Since α is less than 1, this indicates a sublinear response of the detector, which arises due to charge trapping effects influencing the overall photocurrent behavior.[50] This sublinear behavior is also reflected in the photoresponse, where the current first increases and then decays over time, as shown in Figure 5.

4. CONCLUSION

Our study provides a comprehensive evaluation of the response of TiO_2 under X-ray illumination, offering new insights into its suitability as an X-ray detector. By systematically analyzing the response of the device under varying X-ray power levels and fixed bias conditions, we established a clear relationship between photocurrent and X-ray power. This linear response highlights the potential of the device for quantifying X-ray intensity, making it an ideal candidate for applications requiring accuracy and scalability. Moreover, the device demonstrates excellent repeatability, with photocurrent values remaining consistent across multiple measurement cycles. This robustness, combined with rapid response and recovery times, ensures reliable performance in dynamic radiation environments. Such attributes make TiO_2 particularly suitable for applications requiring consistent performance under sustained radiation exposure, including medical imaging, industrial radiography, and space instrumentation. Overall, this work provides valuable insights into TiO_2 as a highly promising material for high-energy radiation detection. Its unique combination of scalability, precision, stability, and fast response establishes a solid foundation for future advancements in X-ray

Table 2. Comparison of Various Parameters for Different Materials

Material	Sensitivity (μ C m Gy^{-1} cm^{-2})	Responsivity (μ C m Gy^{-1})	$\mu\tau$ (cm^2 V^{-1})	References
TiO_2	29.49	1.16×10^{-5} (20 V)	2.77×10^{-6}	This work
Ga_2O_3	138.80 (μ C m Gy^{-1} cm^{-3})	6.8×10^{-4} (200 V)	-	54
Bi_2O_3	1	-	10^{-4}	59
PbI_2-TiO_2	0.5	-	1.21×10^{-6}	60
PbI_2	0.08	-	0.19×10^{-6}	60
PbO	-	-	4.4×10^{-7}	24
α-Selenium	0.02	-	10^{-7}	61
CZT	2.4	-	3.3×10^{-3}	61
$MAPbI_3$ (single crystal)	2.6×10^3	-	1.3×10^{-2}	61

https://doi.org/10.1021/acsaelm.5c00757
ACS Appl. Electron. Mater. 2025, 7, 5322−5330

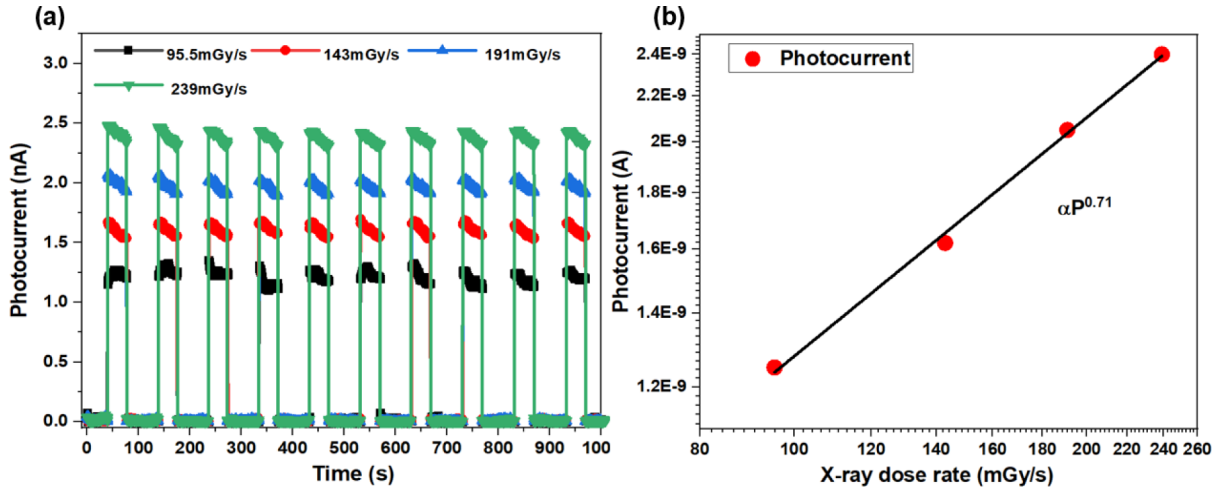

Figure 7. (a) The response of the detector over ten repeated measurement cycles under X-ray exposure at varying dose rates with a fixed bias voltage of 20 V. (b) The response of the detector exhibits a linear dependency with X-ray dose rate.

detection technologies and related high-energy optoelectronic applications.

■ ASSOCIATED CONTENT

Supporting Information

The Supporting Information is available free of charge at https://pubs.acs.org/doi/10.1021/acsaelm.5c00757.

(S1) for measurement detail; (S2) for sensitivity as a function of dose rate (PDF)

■ AUTHOR INFORMATION

Corresponding Author

Parushottam Majhi − *Department of Physics, Indian Institute of Technology Bombay, Mumbai 400076, India;* orcid.org/0009-0009-8391-7300; Email: parushottam.physics@gmail.com, pmajhi@iitb.ac.in

Authors

Rupa Jeena − *Department of Physics, Indian Institute of Technology Bombay, Mumbai 400076, India*

Saikat Mitra − *S. N. Bose National Centre for Basic Sciences, Kolkata 700106, India*

Pankaj Chetry − *IIT Bombay Monash Research Academy, Indian Institute of Technology Bombay, Mumbai 400076, India*

Kantimay Das Gupta − *Department of Physics, Indian Institute of Technology Bombay, Mumbai 400076, India*

Pradeep Sarin − *Department of Physics, Indian Institute of Technology Bombay, Mumbai 400076, India*

Complete contact information is available at: https://pubs.acs.org/10.1021/acsaelm.5c00757

Notes

The authors declare no competing financial interest.

■ ACKNOWLEDGMENTS

The authors thank IIT Bombay, Mumbai, India, for providing access to the fabrication and characterization equipment used in this research work. They extend special thanks to the S. N. Bose National Centre for Basic Sciences, Kolkata, India, and Dr. Saquib Shamim for their help in conducting the experiments on X-ray detection. Rupa Jeena expresses sincere gratitude to the Ministry of Education for supporting the research through the PMRF (Prime Minister's Research Fellowship) program.

■ REFERENCES

(1) Ali, A.; Chiang, Y. W.; Santos, R. M. X-ray diffraction techniques for mineral characterization: A review for engineers of the fundamentals, applications, and research directions. *Minerals* **2022**, *12* (2), 205.

(2) Salvo, L.; Cloetens, P.; Maire, E.; Zabler, S.; Blandin, J. J.; Buffiere, J. Y.; et al. X-ray micro-tomography an attractive characterisation technique in materials science. *Nucl. Instrum. Methods Phys. Res. B: Beam Interact. Mater. At.* **2003**, *200*, 273−286.

(3) Spahn, M. X-ray detectors in medical imaging. *Nucl. Instrum. Methods Phys. Res. A Equip.* **2013**, *731*, 57−63.

(4) Akcay, S.; Breckon, T. Towards automatic threat detection: A survey of advances of deep learning within x-ray security imaging. *Pattern Recognit.* **2022**, *122*, 108245.

(5) Luggar, R.; Gilboy, W. Recent developments in industrial applications of elastic scatter x-ray inspection. *Radiat. Phys. Chem.* **1999**, *56* (1−2), 213−227.

(6) Jin, L.; Jia, W.; Hei, D.; Zhao, L.; Cheng, C. Feasibility study of the high frequency x-ray communication using selective characteristic x-rays. *Opt. Commun.* **2021**, *484*, 126697.

(7) Prekas, G.; Sabet, H.; Bhandari, H.; Derderian, G.; Robertson, F.; Kudrolli, H. Direct and indirect detectors for x-ray photon counting systems.In *2011 IEEE Nuclear Science Symposium Conference Record*2011IEEEpp. 1487−1493

(8) Partridge, M.; Hesse, B. M.; Müller, L. A performance comparison of direct-and indirect-detection flat-panel imagers. *Nucl. Instrum. Methods Phys. Res. A :Accelerators, Spectrometers, Detectors Associated Equip.* **2002**, *484* (1−3), 351−363.

(9) Xu, Y.; Zhou, Q.; Huang, J.; Li, W.; Chen, J.; Wang, K. Highly-sensitive indirect-conversion x-ray detector with an embedded photodiode formed by a three-dimensional dual-gate thin-film transistor. *J. Lightwave Technol.* **2020**, *38* (14), 3775−3780.

(10) Oliveira, J.; Correia, V.; Sowade, E.; Etxebarria, I.; Rodriguez, R. D.; Mitra, K. Y.; et al. Indirect x-ray detectors based on inkjet-printed photodetectors with a screen-printed scintillator layer. *ACS Appl. Mater. Interfaces* **2018**, *10* (15), 12904−12912.

(11) Oliveira, J.; Correia, V.; Costa, P.; Francesko, A.; Rocha, G.; Lanceros-Mendez, S. Stretchable scintillator composites for indirect x-ray detectors. *Composites, Part B* **2018**, *133*, 226−231.

(12) Rowlands, J. A. Material change for x-ray detectors. *Nature* **2017**, *550* (7674), 47−48.

(13) Kasap, S. O.; Rowlands, J. A. Direct-conversion flat-panel x-ray image sensors for digital radiography. *Proc. IEEE* **2002**, *90* (4), 591−604.
(14) Datta, A.; Zhong, Z.; Motakef, S. A new generation of direct x-ray detectors for medical and synchrotron imaging applications. *Sci. Rep.* **2020**, *10* (1), 20097.
(15) Basiricò, L.; Ciavatti, A.; Fraboni, B. Solution-grown organic and perovskite x-ray detectors: A new paradigm for the direct detection of ionizing radiation. *Adv. Mater. Technol.* **2021**, *6* (1), 2000475.
(16) Geng, X.; Chen, Y. A.; Li, Y. Y.; Ren, J.; Dun, G. H.; Qin, K.; Lin, Z.; Peng, J.; Tian, H.; Yang, Y.; et al. Lead-free halide perovskites for direct x-ray detectors. *Adv. Sci.* **2023**, *10* (23), 2300256.
(17) Kasap, S.O.; Kabir, M. Z.; Rowlands, J. Recent advances in x-ray photoconductors for direct conversion x-ray image detectors. *Curr. Appl. Phys.* **2006**, *6* (3), 288−292.
(18) Mitra, S.; Majhi, P.; Maity, A.; Hazra, S.; Chowdhury, A.; Ghosh, B. Direct & efficient detection of x-ray radiation using thermally evaporated 2d hybrid lead halide perovskite (ba2pbbr4)-(ba= n-butylammonium= c4h9nh3) film. *Phys. Scr.* **2024**, *99* (7), 075969.
(19) Tull, C.; Iwanczyk, J.; Patt, B.; Barkan, S.; Feng, L. High efficiency silicon x-ray detectors.*2003 IEEE Nuclear Science Symposium. Conference Record (IEEE Cat. No. 03CH37515)*High efficiency silicon x-ray detectors. *2003 IEEE Nuclear Science Symposium. Conference Record (IEEE Cat. No. 03CH37515)*; IEEE, 2003, Vol. *2*, pp. 1341−1345.
(20) Manzanillas, L.; Aplin, S.; Balerna, A.; Bell, P.; Casas, J.; Cascella, M.; et al. Development of multi-element monolithic germanium detectors for x-ray detection at synchrotron facilities. *Nucl. Instrum. Methods Phys. Res. Aaccelerators, Spectrometers, Detectors Associated Equip.* **2023**, *1047*, 167904.
(21) Huang, H.; Abbaszadeh, S. Recent developments of amorphous selenium-based x-ray detectors: A review. *IEEE Sens. J.* **2020**, *20* (4), 1694−1704.
(22) Kuo, T. T.; Wu, C. M.; Lu, H. H.; Chan, I.; Wang, K.; Leou, K. C. Flexible x-ray imaging detector based on direct conversion in amorphous selenium. *J. Vac. Sci. Technol., A* **2014**, *32* (4), 4.
(23) Kang, S.; Jung, B.; Noh, S.; Cho, C.; Yoon, I.; Park, J. Feasibility study of direct-conversion x-ray detection using cadmium zinc telluride films. *J. Instrum.* **2012**, *7* (1), C01010.
(24) Li, Y.; Wang, X.; Liang, J.; Zhang, L.; Zhang, J. Recent progress in direct x-ray detectors based on metal oxide wide bandgap semiconductors: A review. *IEEE Sensors J.* **2024**, *24* (23), 38569−38583.
(25) Prasad, C. V.; Labed, M.; Shaikh, M. T. A. S.; Min, J. Y.; Nguyen, T. H. V.; Song, W.; Kim, K. J.; Rim, Y. S.; et al. Ga2o3-based x-ray detector and scintillators: A review. *Mater. Today Phys.* **2023**, *35*, 101095.
(26) Zhang, Z.; Chen, M.; Bai, X.; Wang, K.; Chen, H.; Deng, S.; et al. Sensitive direct-conversion x-ray detectors formed by zno nanowire field emitters and β-ga2o3 photoconductor targets with an electron bombardment induced photoconductivity mechanism. *Photonics Res.* **2021**, *9* (12), 2420−2428.
(27) Semeniuk, O.; Grynko, O.; Decrescenzo, G.; Juska, G.; Wang, K.; Reznik, A. Characterization of polycrystalline lead oxide for application in direct conversion x-ray detectors. *Sci. Rep.* **2017**, *7* (1), 8659.
(28) Lee, D.; Lee, K.; Seo, J. High signal-to-noise ratio hgi2 x-ray detector assisted with ultraviolet radiation. *Nucl Instrum.Methods In Phys. Res. Sec A: accelerators, Spectrometers, Detectors Associated Equip.* **2019**, *941*, 162364.
(29) Pettinato, S.; Girolami, M.; Olivieri, R.; Stravato, A.; Caruso, C.; Salvatori, S. A diamond-based dose-per-pulse x-ray detector for radiation therapy. *Materials* **2021**, *14* (18), 5203.
(30) Lees, J.; Bassford, D.; Bunce, E.; Sims, M.; Horsfall, A. Silicon carbide x-ray detectors for planetary exploration. *Nucl. Instru. Methods Phys Research Sect A: Accelerators, Spectrometers, Detectors And Associated Equip.* **2009**, *604* (1−2), 174−176.
(31) Sun, H.; Liu, Y.; Gao, X.; Zhu, X.; Yang, D. Bendable 3d-structured x-ray photodetectors based on pure pbi2 single crystal. *Semicond. Sci. Technol.* **2021**, *36* (3), 035022.
(32) Yu, L.; Pereira, A. L.; Tran, D. N.; Santos, A. M.; Losic, D. Bismuth oxide films for x-ray shielding: Effects of particle size and structural morphology. *Mater. Chem. Phys.* **2021**, *260*, 124084.
(33) Cramer, T.; Fratelli, I.; Barquinha, P.; Santa, A.; Fernandes, C.; D'Annunzio, F.; Loussert, C.; Martins, R.; Fortunato, E.; Fraboni, B.; et al. Passive radiofrequency x-ray dosimeter tag based on flexible radiation-sensitive oxide field-effect transistor. *Sci. Adv.* **2018**, *4* (6), No. eaat1825.
(34) Peiris, S.; de Silva, H. B.; Ranasinghe, K. N.; Bandara, S. V.; Perera, I. R. Recent development and future prospects of tio2 photocatalysis. *J. Chin. Chem. Soc.* **2021**, *68* (5), 738−769.
(35) Matias, M. L.; Pimentel, A.; Reis-Machado, A. S.; Rodrigues, J.; Deuermeier, J.; Fortunato, E.; et al. Enhanced fe-tio2 solar photocatalysts on porous platforms for water purification. *Nanomaterials* **2022**, *12* (6), 1005.
(36) Li, Z.; Li, Z.; Zuo, C.; Fang, X. Application of nanostructured tio2 in uv photodetectors: A review. *Adv. Mater.* **2022**, *34* (28), 2109083.
(37) Xue, H.; Kong, X.; Liu, Z.; Liu, C.; Zhou, J.; Chen, W.; Ruan, S.; Xu, Q. Tio2 based metal-semiconductor-metal ultraviolet photodetectors. *Appl. Phys. Lett.* **2007**, *90* (20), 201118.
(38) Nunes, D.; Fortunato, E.; Martins, R. Flexible nanostructured tio2-based gas and uv sensors: A review. *Discov. Mater.* **2022**, *2* (1), 2.
(39) Žerjav, G.; Žižek, K.; Zavašnik, J.; Pintar, A. Brookite vs. rutile vs. anatase: Whats behind their various photocatalytic activities? *J. Environ. Chem. Eng.* **2022**, *10* (3), 107722.
(40) Allen, N. S.; Mahdjoub, N.; Vishnyakov, V.; Kelly, P. J.; Kriek, R. J. The effect of crystalline phase (anatase, brookite and rutile) and size on the photocatalytic activity of calcined polymorphic titanium dioxide (tio2). *Polym. Degrad. Stab.* **2018**, *150*, 31−36.
(41) Kang, M.; Kim, S. W.; Park, H. Y. Optical properties of tio2 thin films with crystal structure. *J. Phys. Chem. Solids* **2018**, *123*, 266−270.
(42) Sreemany, M.; Sen, S. A simple spectrophotometric method for determination of the optical constants and band gap energy of multiple layer tio2 thin films. *Mater. Chem. Phys.* **2004**, *83* (1), 169−177.
(43) Bento, D. H.; Matias, M. L.; Magalhães, M.; Quitério, C.; Pimentel, A.; Sousa, D.; et al. Self-cleaning stone façades using tio2 microwave-synthesised coatings. *Cleaner Materials* **2025**, *15*, 100294.
(44) Chetry, P.; George, E.; Sarin, P.; Gupta, K. D.; Suresh, K.; Navas, J.; et al. Novel ultraviolet and ionizing radiation detectors made from tio wide-bandgap semiconductor. *IEEE Sens. J.* **2023**, *23* (1), 724−732.
(45) Chen, Y.; Li, Y.; Wu, J.; Duan, W. General criterion to distinguish between schottky and ohmic contacts at the metal/two-dimensional semiconductor interface. *Nanoscale* **2017**, *9* (5), 2068−2073.
(46) Thamaphat, K.; Limsuwan, P.; Ngotawornchai, B. Phase characterization of tio2 powder by xrd and tem. *Agric. Nat. Resour.* **2008**, *42* (5), 357−361.
(47) Bokuniaeva, A.; Vorokh, A. Estimation of particle size using the debye equation and the scherrer formula for polyphasic tio2 powder. *J phys.conf. ser.* **2019**, *1410*, 012057.
(48) Zhang, Y.; Harris, C. X.; Wallenmeyer, P.; Murowchick, J.; Chen, X. Asymmetric lattice vibrational characteristics of rutile tio2 as revealed by laser power dependent raman spectroscopy. *J. Phys. Chem. C* **2013**, *117* (45), 24015−24022.
(49) Khan, M.; Bhatti, K.; Qindeel, R.; Althobaiti, H. S.; Alonizan, N. Structural, electrical and optical properties of multilayer tio2 thin films deposited by sol−gel spin coating. *Results Phys.* **2017**, *7*, 1437−1439.
(50) Yukta; Ghosh, J.; Afroz, M. A.; Alghamdi, S.; Sellin, P.; Satapathi, S. Efficient and highly stable x-ray detection and imaging using 2d (ba) 2pbi4 perovskite single crystals. *ACS Photonics* **2022**, *9* (11), 3529−3539.

https://doi.org/10.1021/acsaelm.5c00757
ACS Appl. Electron. Mater. 2025, 7, 5322−5330

(51) Liu, R.; Li, F.; Zeng, F.; Zhao, R.; Zheng, R. Halide perovskite x-ray detectors: Fundamentals, progress, and outlook. *Appl. Phys. Rev.* **2024**, *11* (2), 2.
(52) Bale, D. S.; Szeles, C. Nature of polarization in wide-bandgap semiconductor detectors under high-flux irradiation: Application to semi-insulating cd 1- x zn x te. *Phys.Rev. B-Condens. Matter.Phys.* **2008**, *77* (3), 035205.
(53) Kozorezov, A.; Gostilo, V.; Owens, A.; Quarati, F.; Shorohov, M.; Webb, M.; Wigmore, J. K.; et al. Polarization effects in thallium bromide x-ray detectors. *J. Appl. Phys.* **2010**, *108* (6), 6.
(54) Chen, M.; Zhang, Z.; Zhan, R.; She, J.; Deng, S.; Xu, N.; et al. Fast-response x-ray detector based on nanocrystalline ga2o3 thin film prepared at room temperature. *Appl. Surf. Sci.* **2021**, *554*, 149619.
(55) Levine, I.; Gupta, S.; Brenner, T. M.; Azulay, D.; Millo, O.; Hodes, G.; et al. Mobility−lifetime products in mapbi3 films. *J. Phys. Chem. Lett.* **2016**, *7* (24), 5219−5226.
(56) Yücel, H.; Birgül, Ö.; Uyar, E.; Çubukçu, Ş. A novel approach in voltage transient technique for the measurement of electron mobility and mobility-lifetime product in cdznte detectors. *Nucl. Eng. Technol.* **2019**, *51* (3), 731−737.
(57) Sellin, P.; Davies, A.; Lohstroh, A.; Ozsan, M.; Parkin, J. Drift mobility and mobility-lifetime products in cdte: Cl grown by the travelling heater method. *IEEE Transactions Nucl. Sci.* **2005**, *52* (6), 3074−3078.
(58) Frohna, K.; Stranks, S. D. *Handbook of Organic Materials for Electronic and Photonic Devices*, Woodhead Publishing Series in Electronic and Optical Materials; 2nd ed.; Ostroverkhova, O., Ed.; Woodhead Publishing, 2019; pp. 211−256.
(59) Mao, L.; Li, Y.; Chen, H.; Yu, L.; Zhang, J. A high-sensitivity flexible direct x-ray detector based on bi2o3/pdms nanocomposite thin film. *Nanomaterials* **2021**, *11* (7), 1832.
(60) Wen, Q.; Ma, W.; Liu, Y.; Jin, X.; Ren, J.; Lin, C. Pbi2−tio2 bulk heterojunctions with long-range ordering for x-ray detectors. *J. Phys. Chem. Lett.* **2021**, *12* (45), 11176−11181.
(61) Yao, F.; Dong, K.; Ke, W.; Fang, G. Micro/nano perovskite materials for advanced x-ray detection and imaging. *ACS Nano* **2024**, *18* (8), 6095−6110.

https://doi.org/10.1021/acsaelm.5c00757
ACS Appl. Electron. Mater. 2025, 7, 5322−5330